European Radiology (2019) 29:3968–3975
https://doi.org/10.1007/s00330-018-5706-6

ONCOLOGY

Differentiation between pilocytic astrocytoma and glioblastoma: a decision tree model using contrast-enhanced magnetic resonance imaging-derived quantitative radiomic features

Fei Dong[1] · Qian Li[1] · Duo Xu[1] · Wenji Xiu[2] · Qiang Zeng[3] · Xiuliang Zhu[1] · Fangfang Xu[1] · Biao Jiang[1] · Minming Zhang[1]

Received: 13 March 2018 / Revised: 8 July 2018 / Accepted: 6 August 2018 / Published online: 12 November 2018

Abstract

Objective To differentiate brain pilocytic astrocytoma (PA) from glioblastoma (GBM) using contrast-enhanced magnetic resonance imaging (MRI) quantitative radiomic features by a decision tree model.

Methods Sixty-six patients from two centres (PA, n = 31; GBM, n = 35) were randomly divided into training and validation data sets (about 2:1). Quantitative radiomic features of the tumours were extracted from contrast-enhanced MR images. A subset of features was selected by feature stability and Boruta algorithm. The selected features were used to build a decision tree model. Predictive accuracy, sensitivity and specificity were used to assess model performance. The classification outcome of the model was combined with tumour location, age and gender features, and multivariable logistic regression analysis and permutation test using the entire data set were performed to further evaluate the decision tree model.

Results A total of 271 radiomic features were successfully extracted for each tumour. Twelve features were selected as input variables to build the decision tree model. Two features S(1, -1) Entropy and S(2, -2) SumAverg were finally included in the model. The model showed an accuracy, sensitivity and specificity of 0.87, 0.90 and 0.83 for the training data set and 0.86, 0.80 and 0.91 for the validation data set. The classification outcome of the model related to the actual tumour types and did not rely on the other three features ($p < 0.001$).

Conclusions A decision tree model with two features derived from the contrast-enhanced MR images performed well in differentiating PA from GBM.

Key Points

- *MRI findings of PA and GBM are sometimes very similar.*
- *Radiomics provides much more quantitative information about tumours.*
- *Radiomic features can help to distinguish PA from GBM.*

Keywords Pilocytic astrocytoma · Glioblastoma · Magnetic resonance imaging · Image enhancement · Decision trees

✉ Qian Li
liqianivy@zju.edu.cn

✉ Minming Zhang
zhangminming@zju.edu.cn

[1] Department of Radiology, the Second Affiliated Hospital, Zhejiang University School of Medicine, Hangzhou 310009, China

[2] Department of Radiology, Fujian Provincial Hospital, Fuzhou 350001, China

[3] Department of Neurosurgery, the Second Affiliated Hospital, Zhejiang University School of Medicine, Hangzhou 310009, China

Abbreviations

CI	Confidence interval
CNS	Central nervous system
CP	Complexity parameter
GBM	Glioblastoma
ICC	Intraclass correlation coefficient
MRI	Magnetic resonance imaging
PA	Pilocytic astrocytoma
ROI	Regions of interest
SD	Standard deviation

Introduction

Pilocytic astrocytoma (PA) is a World Health Organization grade I glioma that accounts for 15.5% of brain and central nervous system (CNS) histologies. PA usually occurs in children and adolescents and has an excellent prognosis after operation [1]. Glioblastoma (GBM) is a World Health Organization grade IV glioma which accounts for 80% of all primary malignant CNS tumours and approximately 54.4% of all malignant gliomas. GBM typically occurs in elderly people and has a very poor prognosis, even with comprehensive treatment [2, 3].

Correct differential diagnosis between PA and GBM is necessary for preoperative decision-making and prognostic evaluation [1, 3–5], and conventional MRI (mainly including T1-weighted imaging, T2-weighted imaging and contrast-enhanced MRI) is widely used. Generally, the typical presentation of tumours can be differentiated by combining patient clinical and imaging information such as age and tumour location. However, the MR imaging findings of brain PA may display a wide spectrum of neuroradiological presentations and resemble those of much more aggressive brain tumours [1] (Fig. 1).

Some functional MR imaging techniques, such as diffusion-weighted imaging and perfusion-weighted imaging, are very useful for differentiating PA from high-grade brain tumours [1]. However, these imaging modalities are not conventionally acquired in some centres initially in a work setting. A more preferable approach would be to deeply analyse and interpret the conventional MR images with some post-processing techniques when needed. Radiomics, which is defined as the conversion of images to higher-dimensional data and the subsequent mining of these data for improved decision support [6], affords such a way to deeply interpret the imaging information [7].

A decision tree is composed of decision rules based on optimal feature cut-off values [8] and has been frequently used for clinical decision-making [8–10].

The aim of this study was to differentiate PA from GBM using radiomic features derived from contrast-enhanced MRI and to build a decision tree model.

Materials and methods

In this study we used data from two centres: centre 1, the Second Affiliated Hospital of Zhejiang University School of Medicine; and centre 2, Fujian Provincial Hospital. The study was approved by the local ethics committee of the two hospitals; patient approval or informed consent for the review of patient images was not required. The overall framework of this study is shown in Fig. 2.

Patients

Sixty patients (30 PAs and 30 GBMs) were included at centre 1. Six cases (1 PA and 5 GBMs) were included at centre 2. Thus, the entire data set comprised 66 patients (35 men and 31 women, 6/27/33 patients assessed using 1.0 T/1.5 T/3.0 T MRI machine, 3/21/42 patients assessed using a Philips/Siemens/GE system). Ages ranged between 8 and 75 years. The inclusion criteria were as follows: (1) availability of clinical information; (2) presurgical MRI scans, including T1-weighted images and post-contrast T1-weighted images; (3) pathologically confirmed PA or GBM; (4) did not receive radiotherapy or chemotherapy before operation. All cases underwent surgical treatment between January 2011 and July 2016. The patients were divided into a training and validation data set with a ratio of about 2:1 with simple randomisation method by R 3.3.1

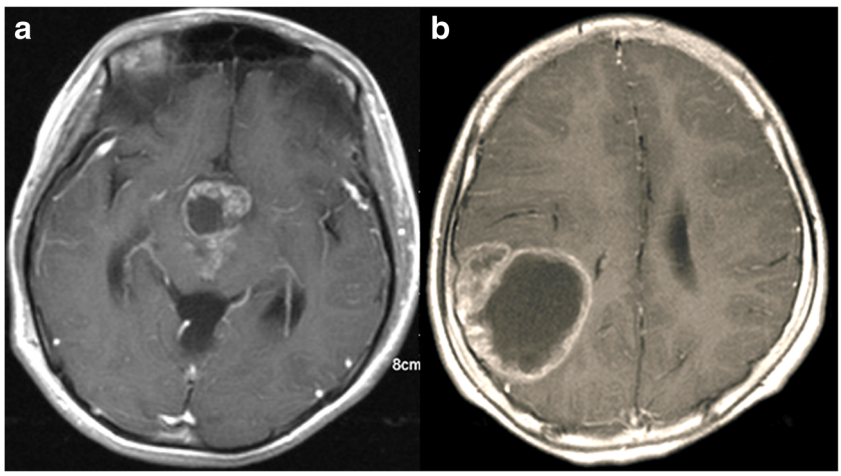

Fig. 1 Case of a 15-year-old girl with pilocytic astrocytoma (**a**) and a 56-year-old man with glioblastoma (**b**). Both cases show cystic solid lesions

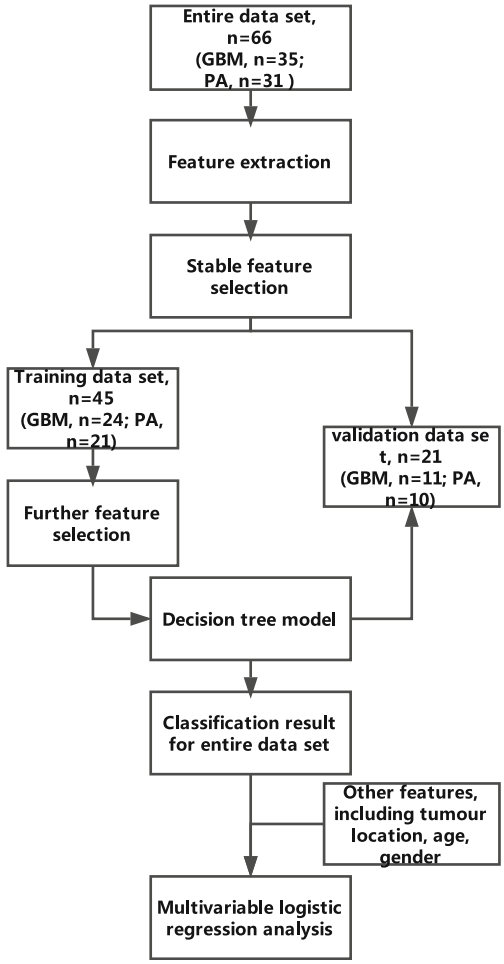

Fig. 2 Overall framework of this study

(http://www.Rproject.org). Patient records and information were de-identified prior to analysis.

MRI parameters

At centre 1, MRI was performed with a 1.0-T Magnetom Expert scanner (Siemens Medical Solutions), 1.5-T Signa Excite scanner (GE Healthcare), 1.5-T Sonata or Aera scanner (Siemens Medical Solutions), 1.5-T Achieva scanner (Philips Healthcare), 3.0-T Discovery 750 scanner (GE Healthcare) and 3.0-T Signa HDxt scanner (GE Healthcare). At centre 2, MRI was performed with a 1.5-T Aera scanner (Siemens Medical Solutions), 1.5-T Achieva scanner (Philips Healthcare) and 3.0-T Verio scanner (Siemens Medical Solutions). All images were acquired using a 6-mm slice thickness, with no slice overlapping. The imaging protocol consisted of either contrast coronal, sagittal and axial T1-weighted imaging. Pre-contrast axial T1-weighted and T2-weighted images were also acquired to improve assessment of the enhanced tumour section. The contrast agents used for the contrast-enhanced MRI sequences were gadodiamide (Omniscan, GE Healthcare) at centre 1 and gadopentetate dimeglumine (Magnevist, Bayer Schering Pharma AG) at centre 2. Both contrast agents were administered by injection though a peripheral venous catheter at a dose that was standardised on the basis of patient body weight (0.2 ml/kg body weight, up to a maximum of 20 ml).

Feature extraction

Features were extracted from contrast-enhanced MR images using MaZda software [11–13]. Before feature extraction, in order to correct the effect of different acquisition protocols and magnetic field strength, the image intensities were normalised (normalisation = 3 sigma, set up in MaZda software) [14]. Extracted features include histogram, gradient, run length matrix (dimension = 6), co-occurrence matrix (dimensions = 6 × 6, distances = 1, 2, 3, 4, 5), autoregressive model and Haar wavelet features. Regions of interest (ROI) were drawn according to the following protocol: (1) in the slice with the maximum tumour enhanced area determined by visual evaluation (F.D., radiologist with 8 years' experience); (2) the ROI was drawn in the largest enhanced part in the selected slice if the tumour had an discontinuous enhancement pattern; (3) thin enhanced cystic wall was excluded in the ROI; (4) the area of each ROI contained no less than 20 metrics and without artefacts (Fig. 3). The ROIs were drawn by two image readers (F.D. and Q.L., radiologists with 8 and 5 years' experience, respectively) together. The two image readers resolved ROI selection disagreements by consensus.

Feature selection

A two-step method was used for feature selection in this study.

First, the stability of the extracted features was evaluated by interobserver reproducibility. Intraclass correlation coefficient (ICC) value was calculated in 10 cases (5 PAs and 5 GBMs, randomly selected using computer-generated random numbers from the entire data set) by three radiologists (F.D., Q.L. and W.X.) for each feature. The features with ICC values of at least 0.9 were selected and considered stable [15].

The Boruta algorithm was then implemented to select the remaining features using the training data set. The Boruta algorithm is a wrapper built around the random forest classification algorithm. The algorithm is configured to explore all possible subsets of the attributes and finally selects the most important variables by comparing the importance of the original attributes with importance achievable at random, estimated using their permuted copies [14, 16]. This algorithm performed well in selecting important features in the prior study [14].

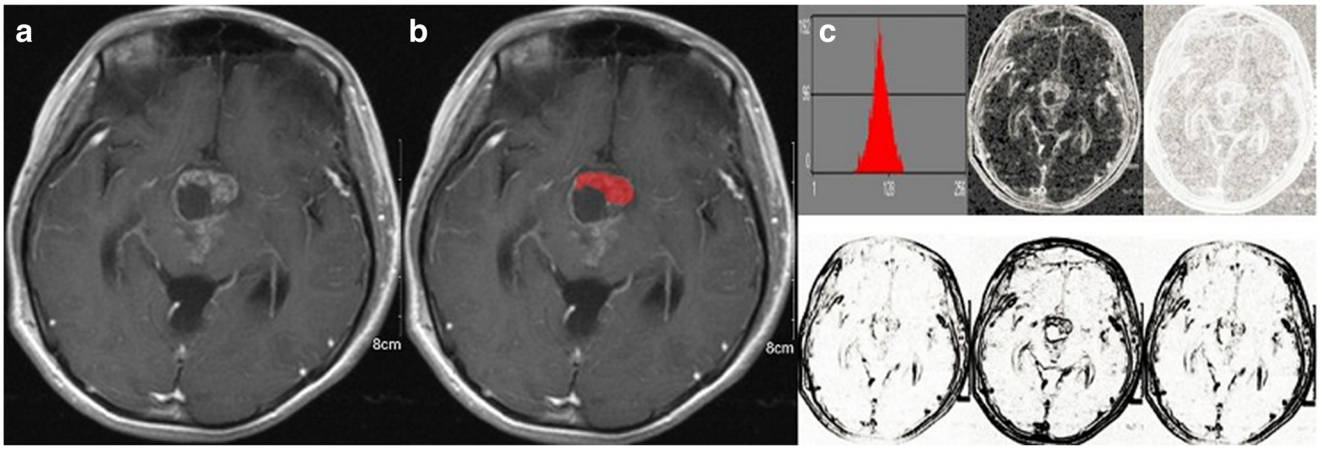

Fig. 3 An example of a selected region of interest (ROI) for a PA case. **a** The raw image. **b** The red area represents the selected ROI. **c** Some of the feature maps generated during features extraction

Decision tree model

With the selected features and training data set, a decision tree model was built using the classification and regression trees (CART) algorithm, which uses a binary recursive process. It is started by splitting subsets of the complete data set (using all predictor variables) into two child nodes repeatedly, and a variety of impurity or diversity measures are used for choosing of the best predictor [17]. In this study, Gini impurity was used for impurity measurement. Complexity parameter (CP) was used to control the tree size. The minimum "xerror" (average of tenfold cross-validation error) was used to select the CP value for building the decision tree model. The model was tested with the validation data set. Accuracy, sensitivity and specificity were used to assess the performance of the model.

Further evaluation of the model

We were interested in finding the performance of the model compared to other traditional features. Then the classification outcome of the model combined with age, location and gender in the entire data set was included in a multivariable logistic regression analysis. Whether the classification outcome of the model was independently correlated with the actual tumour type was tested and the weights of the variables were computed. As the sample size was small, to further test the reliability of the result, a permutation test (with the samples permuted for 1000 times) were performed.

Statistical analysis

The Kolmogorov–Smirnov test was used to test the distribution of age for PA and GBM cases, and the data were presented as mean ± standard deviation (SD) and (or) median according to normal distribution or not. The statistical significance levels were two-sided, with the statistical significance level set at 0.05. The statistical analyses were performed using R software and 'stats' package.

Software package for radiomic data processing

The feature selection and the decision tree model building were performed with the following R packages: 'caret', 'lattice', 'Boruta', 'ranger', 'psy', 'rpart', 'ggplot2'. The decision tree model was plotted mainly based on 'rpart.plot' package.

Results

Patients

In this study, 48.4% (15/31) of PAs occurred in patients 20 and older (between 21 and 68 years of age), 25.8% (8/31) of cases occurred in supratentorial compartment (cerebrum and midbrain) and 22.6% (7/31) of cases occurred both in patients 20 and older and supratentorial compartment. For GBMs, 2.9%

Table 1 Patient gender, age and tumour location characters

		PA	GBM
Sex	Male (*n*)	12	23
	Female (*n*)	19	12
Age	Range (years)	8–68	28–75
	Median (mean ± SD) (years)	19 (26 ± 17)	57 (55 ± 12)
	≤ 19 years (*n*)	16	0
	> 19 years (*n*)	15	35
Location	Supratentorial (*n*)	8	34
	Subtentorial (*n*)	23	1

PA pilocytic astrocytoma, *GBM* glioblastoma multiforme, *SD* standard deviation

Table 2 Extracted features and the description [12, 18]

Feature class	Feature quantity	Feature description
Histogram feature	9	Computed from the intensity of pixels, without taking into consideration spatial relations between the pixels
Co-occurrence matrix feature	220	Computed from intensities of pairs of pixels, the spatial relationship of the two pixels in a pair is defined
Run length matrix feature	20	Counts of pixel runs with the specified greyscale level and length
Gradient feature	5	Derives features from the gradient magnitude map of the image
Autoregressive model-based feature	5	Predicted as a weighted sum of four neighbouring pixel intensities
Wavelet feature	12	Apply the density features on the four wavelet decompositions

(1/35) of cases were located in the subtentorial region (cerebellum). The detailed patient gender, age and tumour location characteristics are listed in Table 1.

Feature extraction and selection

A total of 271 radiomic features were successfully extracted for each tumour. These features include 9 histogram features, 220 co-occurrence matrix features, 20 run length matrix features, 5 gradient features, 5 autoregressive model features and 12 Haar wavelet features (Table 2). Eighty features were considered as stable features with ICC values of at least 0.9. Twelve features were selected by the Boruta algorithm (Fig. 4). The selected features including one histogram feature, the kurtosis, and the following 11 co-occurrence matrix features: S(1,0) Entropy, S(1, 0) SumAverg, S(0, 1) Entropy, S(1, 1) Entropy, S(1,-1) Entropy, S(2, 0) Entropy, S(0, 2) SumAverg, S(0, 2) Entropy, S(2, 2) SumAverg, S(2, -2) SumAverg and S(2, -2) Entropy.

Decision tree model

The decision tree model was fed with the 12 selected features and trained with the training data set. The minimum 'xerror' was 0.429, and a CP value of 0.01 was selected for building the model. Finally, the model was built with two features (Fig. 5). The predictive accuracy of the model was 0.87 for training data set and 0.86 for the validation data set.

Further evaluation of the model

The multivariate logistic regression analysis showed that the classification outcome of the model related to the actual tumour types and did not rely on location, age and gender features ($p < 0.001$). The model showed the largest weight value when compared with other variables (location, age and gender). The results of logistic regression analysis are listed in Table 3

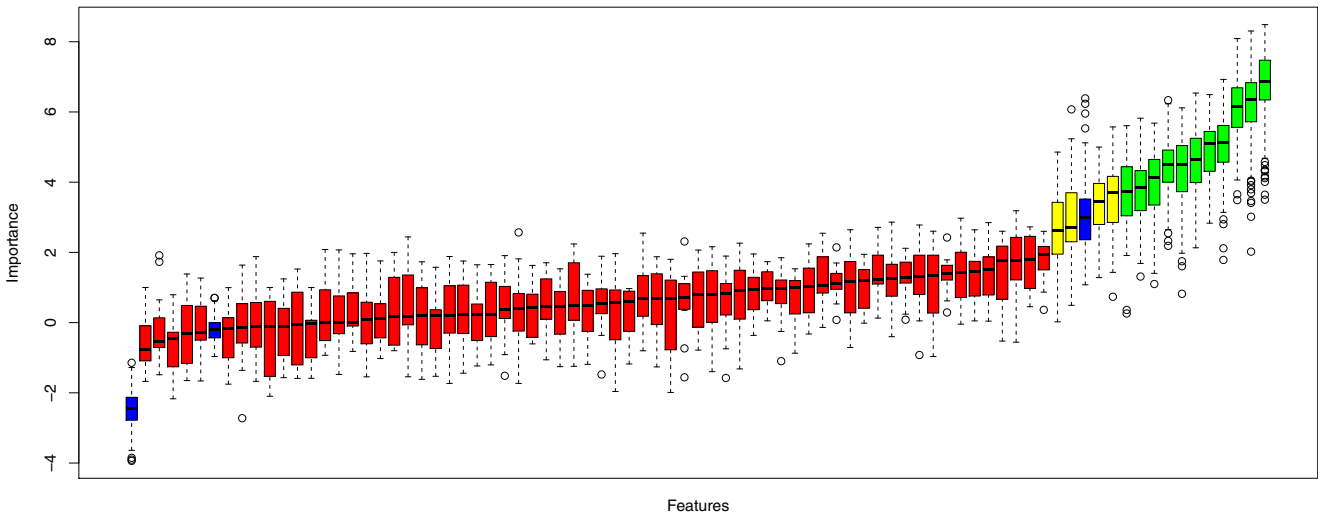

Fig. 4 Feature selection with the Boruta algorithm. Each boxplot represents a feature. Blue boxplots correspond to minimal, average and maximum importance of a shadow feature. Red and green boxplots represent importance of respectively rejected and confirmed features [16]

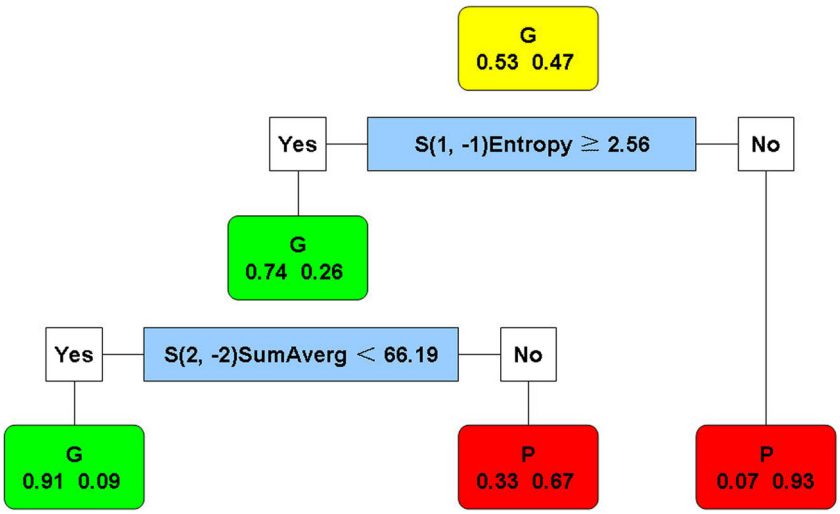

Fig. 5 Decision tree model. For each node, the frame shows the larger proportion tumour (GBM or PA) and the probability per class of tumour in the node (left for GBM, right for PA). Two branches, which represent the classification, derive from the nodes according to the value of features (left for yes, right for no). G, glioblastoma; P, pilocytic astrocytoma

Discussion

Though PA and GBM have different histopathology and contrast enhancement mechanism [1, 19–22], the visual MRI findings are sometimes insufficient to allow their differentiation. In this study, we extracted and selected some enhanced MRI-derived quantitative radiomic features and built a decision tree model to differentiate PA from GBM tumours. We found that a model with two of the radiomic features performed well in doing that.

Prior studies have found that age and tumour location are important features to differentiate PA from GBM. PAs commonly occur in the cerebellum and optic pathway of children and adolescents (0–19 years) [1] and primary GBMs usually occur in the supratentorial compartment of elderly patients [23, 24]. However, there is some overlap of age and location for the two tumours. A large sample analysis showed that 71.8% of PAs occurred in patients 0–19 years old and 28.2% occurred in patients 20 years and older, and the most common location for PAs is the cerebellum (34.3%), followed by cerebrum/lobar (21.7%), brainstem (10.7%), ventricle (6.4%), spinal cord (5.2%) and optic nerve (3%) without regard to age [25]. Also, GBMs have an annual incidence of 1.5 per 1,000,000 in children and can also develop in the cerebellum [24]. This may therefore bring cause difficulties in differentiating the two tumours by only age and tumour location information.

Furthermore, PA has a wide spectrum of neuroradiological presentations [1]. The predominant four imaging patterns of PA in contrast-enhanced MR images include an obvious enhancing nodule with a non-enhancing cyst; an obvious enhancing nodule with an enhancing cyst; a cyst with an internal enhancing part or an enhanced mass with a small cystic part [26, 27]. GBMs in contrast-enhanced MR images usually appear as masses with contrast enhancement at their margin [24]. There is also some overlap in the presentation of the two tumours in enhanced images which may make them difficult to differentiate by visual interpretation.

Radiomics provides a good quantitative representation of the underlying biological information and can be used for diagnosis, prognosis and therapy response evaluation in oncology [28]. Selecting which images to use is usually the basis for a radiomic study. In fact, the imaging sequences and modalities used for radiomics studies vary in current literature [29, 30]. In spite of more sequences and modality images that can afford more information, we think that it may be more effective to select fewer but more specific images. In this study, only contrast-enhanced MR images were used for two main reasons. Firstly, contrast-enhanced MR images were conveniently available and usually clinically used for brain tumour diagnosis and evaluation. Secondly, the histopathology and contrast-enhanced mechanism were different for the two tumours [1, 19–22].

The decision model works well in this study despite the acquisition parameters of images not being uniform and despite us not using a very thin thickness. In fact, the uniform acquisition parameters and a slice thickness about 5 mm are common in current radiomic studies [31–35]. It is likely that

Table 3 Results of multivariate logistic regression analysis

Variables	coefficient	*p* value
Classification outcome of the model	0.401	< 0.001
Location	0.347	< 0.001
Age	0.006	0.011
Gender	-0.068	0.170

The classification outcome of the model relates to the actual tumour types and does not rely on the other three features

the method would work better with uniform acquisition settings and proper slice thickness [6].

Most of the selected features and both of the final model-building features in this study were co-occurrence matrix features. The co-occurrence matrix features are computed from pixel pair intensities, and the spatial relationship of the two pixels in a pair is considered [13]. A recent study found that co-occurring gradients in MR imaging were useful for distinguishing brain tumour subtypes [36]. In this study, it may indicate that these selected co-occurrence matrix features have some relationship with the enhancement difference of PA and GBM.

We provided a decision tree model for differentiating PA from GBM in this study. The model included only two radiomic features but achieved a high accuracy. Some limitations should also be considered. First, this study included a small number of subjects, and the prospective confirmation of the model in our study with a larger sample size is needed. Second, to get a more stable model, we used data from two centres and with different contrast agents, but the data were unbalanced.

Conclusions

Our study showed a decision tree model with two features extracted from enhanced MR images performed well in differentiating PA from GBM. This model provides an objective diagnostic method to differentiate PA from GBM, and it may be especially helpful for those cases that are difficult to distinguish by conventional interpretation approaches that mainly depend on age and location features.

Funding This study has received funding by the medicine and health scientific and technological program of Zhejiang province, China (2016KYA104 and 2017KY374)

Compliance with ethical standards

Guarantor The scientific guarantor of this publication is Minming Zhang.

Conflict of interest The authors of this manuscript declare no relationships with any companies whose products or services may be related to the subject matter of the article.

Statistics and biometry One of the authors has significant statistical expertise.

Informed consent Written informed consent was not required for this study because this is a retrospective study on the images.

Ethical approval Institutional review board approval was obtained.

Methodology
- retrospective
- diagnostic or prognostic study
- multicentre study

References

1. Gaudino S, Martucci M, Russo R et al (2017) MR imaging of brain pilocytic astrocytoma: beyond the stereotype of benign astrocytoma. Childs Nerv Syst 33:35–54
2. Thorne AH, Zanca C, Furnari F (2016) Epidermal growth factor receptor targeting and challenges in glioblastoma. Neuro Oncol 18:914–918
3. Alifieris C, Trafalis DT (2015) Glioblastoma multiforme: pathogenesis and treatment. Pharmacol Ther 152:63–82
4. Alford R, Gargan L, Bowers DC, Klesse LJ, Weprin B, Koral K (2016) Postoperative surveillance of pediatric cerebellar pilocytic astrocytoma. J Neurooncol 130:149–154
5. Cykowski MD, Allen RA, Kanaly AC et al (2013) The differential diagnosis of pilocytic astrocytoma with atypical features and malignant glioma: an analysis of 16 cases with emphasis on distinguishing molecular features. J Neurooncol 115:477–486
6. Gillies RJ, Kinahan PE, Hricak H (2016) Radiomics: images are more than pictures, they are data. Radiology 278:563–577
7. Yip SS, Aerts HJ (2016) Applications and limitations of radiomics. Phys Med Biol 61:R150–R166
8. Rau CS, Wu SC, Chien PC et al (2018) Identification of pancreatic injury in patients with elevated amylase or lipase level using a decision tree classifier: a cross-sectional retrospective analysis in a level I trauma center. Int J Environ Res Public Health. https://doi.org/10.3390/ijerph15020277
9. El Hentour K, Millet I, Pages-Bouic E, Curros-Doyon F, Molinari N, Taourel P (2018) How to differentiate acute pelvic inflammatory disease from acute appendicitis ? A decision tree based on CT findings. Eur Radiol 28:673–682
10. Zimmerman RK, Balasubramani GK, Nowalk MP et al (2016) Classification and regression tree (CART) analysis to predict influenza in primary care patients. BMC Infect Dis 16:503
11. Strzelecki M, Szczypinski P, Materka A, Klepaczko A (2013) A software tool for automatic classification and segmentation of 2D/3D medical images. Nucl Instrum Methods Phys Res 702:137–140
12. Szczypiński PM, Strzelecki M, Materka A, Klepaczko A (2009) MaZda–a software package for image texture analysis. Comput Methods Programs Biomed 94:66–76
13. Szczypiński PM, Strzelecki M, Materka A (2007) MaZda–a software for texture analysis. Proc of ISITC, Republic of Korea, p 245–249
14. Baessler B, Mannil M, Oebel S, Maintz D, Alkadhi H, Manka R (2018) Subacute and chronic left ventricular myocardial scar: accuracy of texture analysis on nonenhanced cine MR images. Radiology 286:103–112
15. Yuan M, Zhang YD, Pu XH et al (2017) Comparison of a radiomic biomarker with volumetric analysis for decoding tumour phenotypes of lung adenocarcinoma with different disease-specific survival. Eur Radiol 27:4857–4865
16. Kursa MB, Rudnicki WR (2010) Feature selection with the Boruta package. J Stat Softw 36:1–13
17. Khalkhali HR, Lotfnezhad Afshar H, Esnaashari O, Jabbari N (2016) Applying data mining techniques to extract hidden patterns about breast cancer survival in an Iranian cohort study. J Res Health Sci 16:31–35
18. Tempany CM, Zou KH, Silverman SG, Brown DL, Kurtz AB, McNeil BJ (2000) Staging of advanced ovarian cancer: comparison of imaging modalities–report from the Radiological Diagnostic Oncology Group. Radiology 215:761–767
19. Collins VP, Jones DT, Giannini C (2015) Pilocytic astrocytoma: pathology, molecular mechanisms and markers. Acta Neuropathol 129:775–788
20. Sato K, Rorke LB (1989) Vascular bundles and wickerworks in childhood brain tumors. Pediatr Neurosci 15:105–110

21. Smirniotopoulos JG, Murphy FM, Rushing EJ, Rees JH, Schroeder JW (2007) Patterns of contrast enhancement in the brain and meninges. Radiographics 27:525–551
22. Aldape K, Zadeh G, Mansouri S, Reifenberger G, von Deimling A (2015) Glioblastoma: pathology, molecular mechanisms and markers. Acta Neuropathol 129:829–848
23. Crespo I, Vital AL, Gonzalez-Tablas M et al (2015) Molecular and genomic alterations in glioblastoma multiforme. Am J Pathol 185: 1820–1833
24. Wirsching HG, Galanis E, Weller M (2016) Glioblastoma. Handb Clin Neurol 134:381–397
25. Johnson DR, Brown PD, Galanis E, Hammack JE (2012) Pilocytic astrocytoma survival in adults: analysis of the Surveillance, Epidemiology, and End Results Program of the National Cancer Institute. J Neurooncol 108:187–193
26. Cyrine S, Sonia Z, Mounir T et al (2013) Pilocytic astrocytoma: a retrospective study of 32 cases. Clin Neurol Neurosurg 115:1220–1225
27. Murray RD, Penar PL, Filippi CG, Tarasiewicz I (2011) Radiographically distinct variant of pilocytic astrocytoma: a case series. J Comput Assist Tomogr 35:495–497
28. Zhou M, Scott J, Chaudhury B et al (2018) Radiomics in brain tumor: image assessment, quantitative feature descriptors, and machine-learning approaches. AJNR Am J Neuroradiol 39:208–216
29. Narang S, Lehrer M, Yang D, Lee J, Rao A (2016) Radiomics in glioblastoma: current status, challenges and potential opportunities. Transl Cancer Res 5:383–397
30. Avanzo M, Stancanello J, El Naqa I (2017) Beyond imaging: the promise of radiomics. Phys Med 38:122–139
31. Shofty B, Artzi M, Ben Bashat D et al (2018) MRI radiomics analysis of molecular alterations in low-grade gliomas. Int J Comput Assist Radiol Surg 13:563–571
32. Li ZC, Bai H, Sun Q et al (2018) Multiregional radiomics features from multiparametric MRI for prediction of MGMT methylation status in glioblastoma multiforme: a multicentre study. Eur Radiol. https://doi.org/10.1007/s00330-017-5302-1
33. Zhang Z, Yang J, Ho A et al (2018) A predictive model for distinguishing radiation necrosis from tumour progression after gamma knife radiosurgery based on radiomic features from MR images. Eur Radiol 28:2255–2263
34. Li Y, Liu X, Qian Z et al (2018) Genotype prediction of ATRX mutation in lower-grade gliomas using an MRI radiomics signature. Eur Radiol 28:2960–2968
35. Zhang X, Tian Q, Wang L et al (2018) Radiomics strategy for molecular subtype stratification of lower-grade glioma: detecting IDH and TP53 Mutations based on multimodal MRI. J Magn Reson Imaging. https://doi.org/10.1002/jmri.25960
36. Prasanna P, Tiwari P, Madabhushi A (2014) Co-occurrence of local anisotropic gradient orientations (CoLIAGe): distinguishing tumor confounders and molecular subtypes on MRI. Med Image Comput Comput Assist Interv 17:73–80